Geophysical Research Letters

RESEARCH LETTER
10.1029/2019GL086778

High-Order Solar Migrating Tides Quench at SSW Onsets

Maosheng He[1], Jeffrey M. Forbes[2], Jorge L. Chau[1], Guozhu Li[3], Weixing Wan[3], and Dmitry V. Korotyshkin[4]

[1]Leibniz-Institute of Atmospheric Physics at the Rostock University, Kühlungsborn, Germany, [2]Ann and H.J. Smead Department of Aerospace Engineering Sciences, University of Colorado Boulder, Boulder, CO, USA, [3]Key Laboratory of Earth and Planetary Physics, Institute of Geology and Geophysics, Chinese Academy of Sciences, Beijing, China, [4]Kazan Federal University, Kazan, Russia

Key Points:
- First six solar tidal harmonics occur in the mesospheric wind during SSW 2018 among which the fourth, fifth, and sixth harmonics quench at the SSW onset
- Wave number diagnosis using multistation techniques suggests that all six harmonics are dominated by migrating tides
- In a near-12-year statistics, the six harmonics and quenching also occur

Supporting Information:
- Supporting Information S1

Correspondence to:
M. He,
he@iap-kborn.de

Citation:
He, M., Forbes, J. M., Chau, J. L., Li, G., Wan, W., & Korotyshkin, D. V. (2020). High-order solar migrating tides quench at SSW onsets. *Geophysical Research Letters*, *47*, e2019GL086778. https://doi.org/10.1029/2019GL086778

Received 20 DEC 2019
Accepted 26 FEB 2020
Accepted article online 29 FEB 2020

Abstract Sudden stratospheric warming events (SSWs) are the most spectacular atmospheric vertical coupling processes, well-known for being associated with diverse wave activities in the upper atmosphere and ionosphere. The first four solar tidal harmonics have been reported as being engaged. Here, combining mesospheric winds detected by three midlatitude radars, we demonstrate at least the first six harmonics that occurred during SSW 2018. Wave number diagnosis demonstrates that all six harmonics are dominated by migrating components. Wavelet analyses reveal that the fourth, fifth, and sixth harmonics quench after the SSW onset. The six harmonics and the quenching appear also in a statistical analysis based on near-12-year observations from one of the radars. We attribute the quenching to reversal of the background eastward wind.

Plain Language Summary Solar tides are the most predictably occurring waves in the upper atmosphere. Although the dynamical theory can be dated back to Laplace in the sixteenth century, upper atmospheric tides were rarely studied observationally until satellites and ground-based radars became common. To date, observational studies have mainly dealt with low-order solar-day harmonics. Here, we combine mesospheric wind observations from three longitudinal sectors to investigate high-order harmonics. Results illustrate that the first six harmonics appear in early 2018, all of which are dominated by Sun-synchronous components. Among these harmonics, the fourth, fifth, and sixth quench at the sudden stratospheric warming onset, which we attribute to variations in the background zonal wind.

1. Introduction

Solar tides are excited by heating due to the diurnal cycle of solar radiation absorption by various chemical species throughout the atmosphere, as well as the release of latent heat associated with convection in the troposphere. There is also substantial evidence that solar tides can also be produced by nonlinear interactions between various tidal components, and between tides and stationary planetary waves. Readers are referred to Truskowski et al. (2014) for a review of how various observed migrating (Sun-synchronous) and nonmigrating tides are thought to be excited. The diurnal cycle of heating generates a series of solar harmonics (designated in this paper as S1, S2, … , S7 corresponding to periods of 24, 12, … , 24/7 hr). Harmonics at least up to S7 were observed in the low atmospheric meteorological observations (e.g., Hedlin et al., 2018), most of which exist also in the upper atmosphere as illustrated in the power spectral density of multiyear observations of midlatitude mesospheric wind, in Figure S1 in the supporting information. Based on numerous modeling efforts and data analyses since the early work of Lindzen and Hong (1974), it is now known that at least for S1 to S4 the atmosphere responds in a quasi-linear fashion to each of these harmonics separately.

Most of the tidal literature is devoted to data analyses, modeling, and interpretation of S1, S2, and S3. Recently, S4 has received some attention in terms of ground-based observations (e.g., Guharay et al., 2018; Jacobi et al., 2017; Smith et al., 2004), space-based observations (e.g., Azeem et al., 2016; Liu et al., 2015; Xu et al., 2012) and modeling (e.g., Geissler et al., 2019; Smith et al., 2004). The ground-based observations have the advantage of high temporal resolution, but cannot distinguish between migrating and nonmigrating tidal components from single-station measurements. On the other hand, tidal determinations from single-spacecraft observations provide a global view but one that is typically an average over periods of order

30–60 days, and thus subject to underestimation due to phase cancellation effects. With respect to harmonics at higher orders, to our knowledge, the only modeling and observational investigation pertaining to S5 and S6 was performed by Miyoshi et al. (2009) in the context of solar terminator waves.

In the present paper we employ a special technique to identify migrating tides from three radars separated in longitude at a near-constant latitude of ~55°N, and thus eliminate some of the shortcomings noted above. We furthermore pursue this in the context of the behaviors of S2–S6 during the stratosphere sudden warming (SSW) of 2018. SSWs are the most spectacular meteorological processes of the atmospheric vertical coupling, in which the polar vortex is destroyed in a couple of days (e.g., Reed, 1963; Scherhag, 1952). SSWs are associated with diverse wave activities in the upper atmosphere and ionosphere, including planetary waves, gravity waves, and lunar and solar tides (e.g., Chau et al., 2012; Pedatella & Forbes, 2010). Among the solar tides, variations of the first four harmonics were reported, among which S2 has attracted most intensive attention. The results of S2 exhibited deep contradictions. Simulations from TIMEGCM (Liu et al., 2010; Pedatella et al., 2014) and WAN (Fuller-Rowell et al., 2011) suggested S2 enhancement and weakening during SSWs, respectively. Single-station analyses in case studies suggested that S2 enhanced at low latitude (Sridharan et al., 2012) but weakened at middle and high latitude (e.g., He et al., 2017). Multistation studies with zonal wave number constraints specified that the S2 migrating component weakens and that two nonmigrating components do not enhance statistically (He & Chau, 2019; Hibbins et al., 2019), which is inconsistent with earlier studies reporting enhancements of all three components (e.g., Smith, 2012; Xiong et al., 2013). The contradiction on the nonmigrating components was reconciled recently by the suggestion that the enhancements are aliasing from secondary waves of nonlinear interactions between the S2 migrating component and traveling planetary waves (He, Chau, Stober et al. 2018; He, Chau, Hall et al. 2018; He & Chau, 2019). To reconcile further the contradictions entail careful comparisons of the tidal evolution under different geophysical conditions, for example, latitude, altitude, SSW stage (before and after onsets), SSW occurring date, and SSW category.

In addition to the responses of S2, enhancements of S1, S3, and S4 were also reported during SSWs (e.g., Gong & Zhou, 2011; Gong et al., 2018; Sathishkumar & Sridharan, 2013, respectively). These enhancements were detected using single-station approaches and therefore it is still not clear that are they associated with migrating or nonmigrating components. The first purpose of the current work is to implement the multistation approach to diagnose the zonal wave numbers of these tidal signatures during SSWs. We also aim to explore the behaviors of higher-order solar tidal harmonics during SSWs.

For the above purposes, we investigate the mesospheric wind observations collected by three meteor radars in three longitudinal sectors during SSW 2018. Figure S2 in the supporting information displays the distribution of the radars, at Juliusruh (54.6°N, 13.4°E), Mohe (53.5°N, 122.3°E), and Kazan (55.7°N, 49°E) (readers are referred to Korotyshkin et al., 2019; Singer et al., 2013; Yu et al., 2013, for the radar frequencies, antenna configurations, and other setups). Combining three radars allows us to diagnose the horizontal scale of the tides. Among the radars, the one at Juliusruh collected continuous observations for more than 12 years, which will be used for a multiyear statistic study.

2. Results

In section 2.1, we diagnose the dominant zonal wave number of tidal harmonics in SSW 2018 through a phase differencing approach (developed in He, Chau, Stober et al., 2018) and explore the temporal evolution of the harmonics during SSWs through wavelet analysis in section 2.2.

2.1. Zonal Wave Number Diagnosis

Figure 1a displays the Lomb-Scargle spectra (Lomb, 1976) of the zonal wind at 90-km altitude during SSW 2018, between 30 November 2017 and 15 February 2018. The three colors represent the three radars. At the first six harmonics, f=1,2, … ,6 cpd, peaks occur above the significance level $\alpha = 0.01$. At each individual harmonic the three complex amplitudes are combined to diagnose the zonal wave number m of the underlying wave through two approaches, the dual- and triple-station approaches detailed in sections A.1 and A.2, respectively. The corresponding dual- and triple-station results are denoted as $\hat{m}_k^D$ (k = 1,2,3 denotes three combinations of radar pairs) and $\hat{m}^T$, illustrated in Figure 1b as the colored and white symbols, respectively. The shape of the colored symbols represents different whole cycles in-between each radar pair.

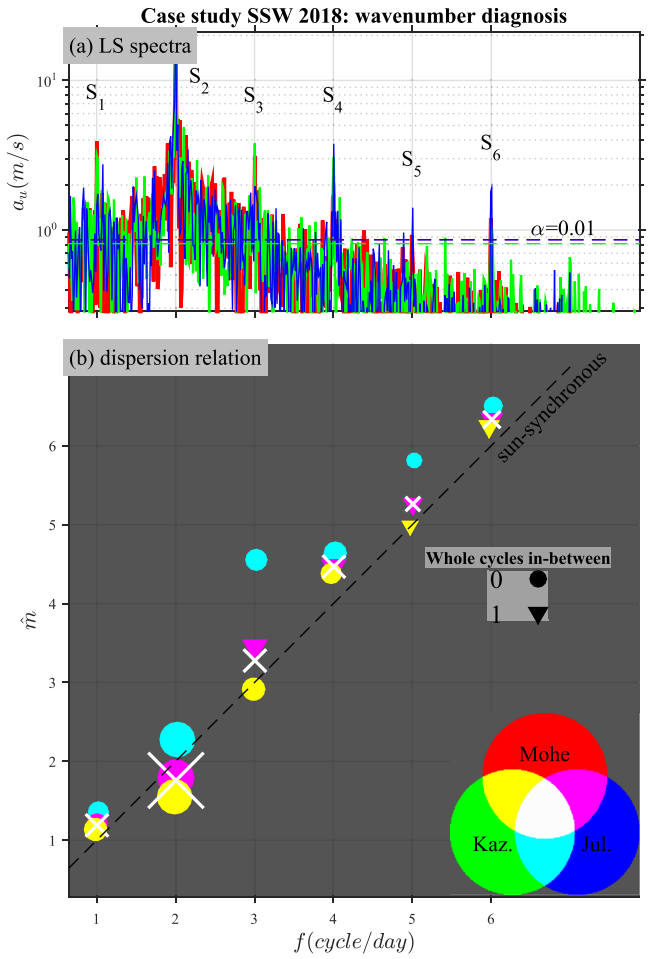

Figure 1. (a) Lomb-Scargle (LS) periodograms of the mesospheric zonal wind over Mohe, Kazan, and Juliusruh, at 90 km altitude between 30 November 2017 and 15 February 2018. (b) Dispersion relation of oscillations at periods of solar-day harmonics through dual-station PDT (colored elements) and triple-station LS approach (white crosses). In (a), the horizontal lines indicate the significance level $\alpha = 0.01$. In (b), the black dashed line represents the phase velocity $v_p = f/m = 360°$/day in longitude. Referring to the color code on the right bottom corner of (b), the primary colors (red, green, and blue in (a)) and their secondary colors (cyan, magenta, and yellow in (b)) denote three single radars and three of their pairs, respectively. In (b), the size of the colored and white symbols represents the product of amplitudes of the two and three relevant spectral peaks from (a), respectively.

For example, the longitudinal separation between Kazan and Juliusruh is shorter than wavelengths at all harmonics, whereas that between Mohe and Juliusruh is shorter than the wavelengths only at the first two harmonics. In Figure 1b, the black dashed line denotes the isoline of Sun-synchronous phase velocity $v_p \equiv f/m = \Omega := 1$cpd. The estimated wavenumber $\hat{m}_k^D(f)$ and $\hat{m}^T(f)$ consistently distribute along the dashed line, suggesting that the underlying waves at all harmonics are dominantly Sun-synchronous, namely, migrating components associated with zonal wave number $m_s(f) = f/\Omega$.

2.2. Quenching of High-Order Tidal Harmonics During SSW

The current section investigates the temporal evolution of the harmonics in early 2018. We carry out Morlet wavelet at each altitude and station and average the resultant spectra in the altitude range $80 < h < 100$ km. The average spectra for the three radars are displayed in Figures 2a–2c, respectively. The spectra share the following characteristics. S2 is almost always the most dominant harmonic, whereas S3–S6 also occur unstably with short time variabilities. The variabilities are potentially due to interactions with planetary waves (e.g., He et al., 2017; Pancheva et al., 2002), gravity waves (e.g., Miyahara & Forbes, 1991) or other tidal components (e.g., Lilienthal & Jacobi, 2019). The high-order harmonics, e.g., S4–S6, occur stronger or more often before the SSW onset (displayed as the magenta line, referring to the central day of polar vortex weakening (PVW), cf., Siddiqui et al., 2015; Zhang & Forbes, 2014) than after the onset. For comparison, the three spectra are averaged in two time windows displayed by the blue and red horizontal bars before and after the onset in Figures 2a–2c. The average, displayed in Figure 2e, exhibits the most significant difference at S4–S6 which are suppressed or quenched after the onset. S6 quenches by about 2/3 according to the ratio shown in Figure 2f.

For a statistical perspective, the same wavelet analysis is implemented on the near-12-year data used in Figure S1, generating an altitude-averaged spectrum similar to Figure 2c but for the period between 30 November 2007 and 15 February 2019. The spectral intensity is averaged with respect to all SSW onsets (referring to PVWs as specified in Table S1 in the supporting information). Such an average is called composite analysis (CA) or superposed epoch analysis. The CA result is displayed in Figure 3a, and its altitude structure, averaged within the time window indicated by the blue horizontal bar in Figure 3a, is displayed in Figure 3b. Similar to Figures 2a–2c, in Figures 3a and 3b the first six harmonics occur, all of which increase with altitude exponentially. Among the harmonics, S4–S6 quench or weaken around the onset. In addition to the quenched harmonics, S2 exhibits, in both Figures 2e and 3c, a weakening after the onset, which is out of our focus hereafter given that the S2 weakening has been reported and discussed individually (Hibbins et al., 2019; He & Chau, 2019).

3. Discussions

In this paper we report the quenching of high-order migrating tides in connection with SSW onset. The existence of migrating tides under undisturbed winter conditions at middle to high latitudes is not surprising. Linear tidal modeling of S2 taking into account forcing by ozone heating alone (Hagan et al., 1999) shows that the tidal amplitudes in zonal wind are significantly enhanced between 75 and 100 km at the poleward of 30° latitude in the winter hemisphere (January and July for the Northern and Southern Hemispheres, respectively) compared to the summer hemisphere where the maximum heating occurs. This is due in part to the Doppler shifting of westward propagating waves to higher frequencies as they preferentially propagate

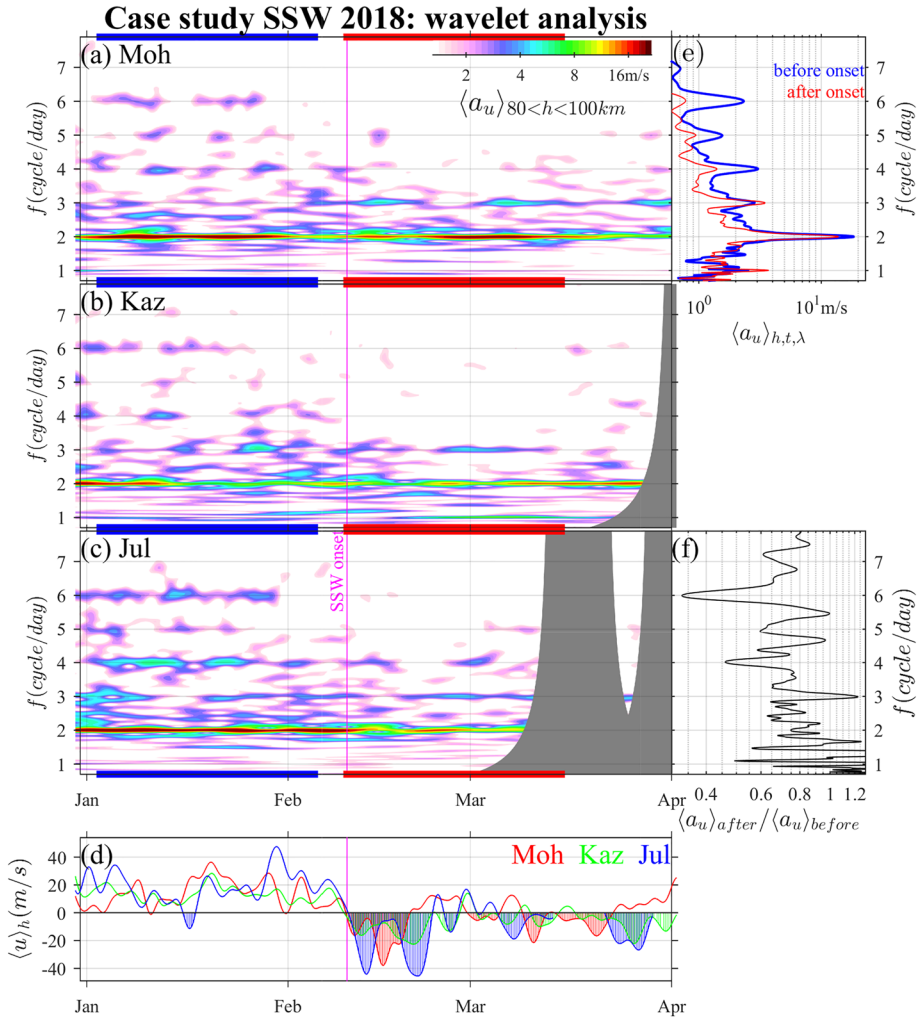

Figure 2. Wavelet spectra of the mesospheric zonal wind over (a) Mohe, (b) Kazan, and (c) Juliusruh, in early 2018. (d) Low-pass filtered zonal wind. (e) Temporal average of the three spectra in (a–c) within the time windows color indicated by the blue and red segments in (a–c). (f) The ratio of the read of the red line over that of the blue in (e). Panels (a–d) are the average of the corresponding results at individual attitudes between 80 and 100 km.

through prevailing eastward winds with reduced susceptibility to dissipation, and with the Doppler-shifting effect increasing with zonal wave number. Winter maxima are in fact revealed for S2–S6 in Figure 4, which displays the similar plot as Figure 3a, but averaged with respect to calendar date. The existence of significant amplitudes for S2 and S3 during nonwinter months in Figure 4 likely reflects the importance of tropospheric sources and tide-tide nonlinear interactions, which were not considered by Hagan et al. (1999). In addition, ozone heating also plays a role. As shown by Xu et al. (2012), while maximum forcing of S2 and S4 occur in the winter hemisphere, that of S3 occurs in the summer hemisphere.

The above simple picture of seasonal variations is significantly disrupted during SSWs, potentially due to changes in the background zonal flow. At progressively higher latitudes, the westward zonal phase speed of migrating tides is lower, leading to stronger potential effects that enter through the Doppler-shifted frequency. According to extensions of tidal theory that investigate the influences of mean winds, dissipation and refraction on the propagation of migrating tides (Forbes and Vincent, 1989; Riggin et al., 2003), a transition from eastward to westward background winds ought to result in some suppression of migrating tides. In the mesosphere and upper stratosphere at boreal middle and high latitudes, the zonal flow is in fact prevailing eastward before SSWs and reverses to westward during SSWs (e.g., Limpasuvan et al., 2016; Pedatella et al., 2014; Siddiqui et al., 2020; Zülicke & Becker, 2013). This is also true in the present context, as illustrated by the low-passed filtered upper mesospheric zonal winds displayed in Figure 2d. At all radars, the

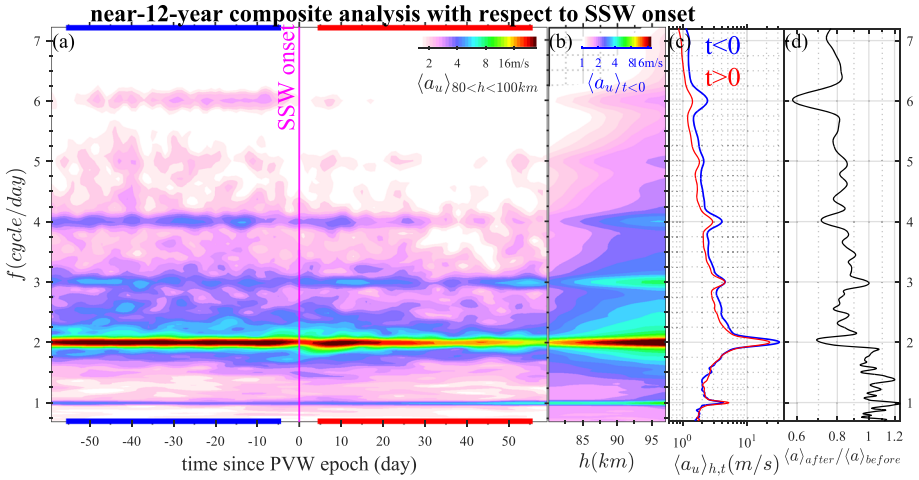

Figure 3. (a) Composite analysis of altitude-averaged (over 80–100 km) wavelet spectrum of the zonal wind over Juliusruh with respect to SSW onsets referring to the PVWs. (b) The wavelet spectrum averaged in the time window indicated by the blue lines before the onset in (a). (c) Temporal average of (a) within the time window indicated by the blue and red lines in (a). (d) The ratio between the red and the blue lines in (d).

wind is eastward before the onset but westward after that, and decreases by 40–60 m/s from the maximum before the onset to the minimum after the onset. The reversal might account for the fact that in Figures 2e and 3c the spectral density, not only at the quenched tidal frequencies but in the whole range $f > 3$ cpd, is stronger before the onset than after. This fact suggests that other westward-propagating waves existing before the onset, for example, gravity waves, might also quench after the onset. However, quantification by modeling that focuses specifically on Doppler-shifting effects on migrating tides at middle to high latitudes is required before more definitive interpretations can be made.

The eastward wind reversal had been used to explain the S2 weakening after SSW onset (Hibbins et al., 2019). The S2 weakening, in Figure 3d, occurs over the long time scale of two months, during which the weakening might be partially attributable to behaviors described traditionally in terms of seasonal variations (e.g., Conte et al., 2018; He & Chau, 2019). Besides the long time scale, on a shorter time scale, S2 also exhibits a weakening, namely, S2 minimizes exactly at the onset lasting less than 10 days in Figure 3a. This minimum was also reported in a case study on SSW 2009 at high latitude and a multiyear statistical study at midlatitude (He et al., 2017; He & Chau, 2019), which was attributed to energy exports in nonlinear interactions with planetary waves through the mechanism of planetary wave amplification by stimulated tidal decay. While our S2 weakening result is consistent with some abovementioned observational studies (He et al., 2017; He & Chau, 2019; Hibbins et al., 2019), it looks contrary to some reports of S2 enhancements during SSWs (e.g., Sridharan et al., 2012). The contradiction is potentially due to the fact that the enhancement and weakening are referring to different SSW stages, and time scales. The weakening might correspond partially to the decline stage of the enhancement. The enhancement was explained in terms of changes in ozone density

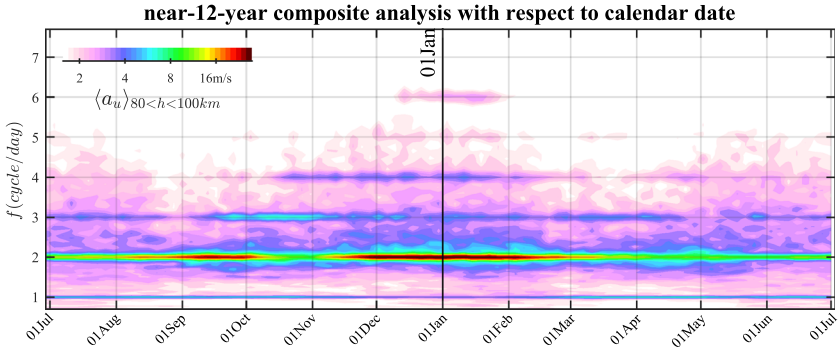

Figure 4. Same as in Figure 3a but averaged with respect to calendar date.

accompanied by tidal heating (Goncharenko et al., 2012; Limpasuvan et al., 2016; Siddiqui et al., 2020). Evaluation of the roles of ozone heating and wind variations on the high-order tidal harmonics during SSWs would benefit from global-scale modeling focused on this topic.

4. Summary

The current work investigates high order solar tidal harmonics in the midlatitude mesospheric wind during SSWs. We present a case study of SSW 2018 using zonal wind observations from three longitudinal sectors and a statistic study using near-12 year of observations from a single station. In both studies, the first six harmonics occur, among which S4–S6 signatures enhance before SSW onset and quench at the onset, potentially due to the enhancement and reversal of eastward mean flow during SSWs. In the case study and using multistation approaches, our wave number diagnosis illustrates that the dominant components of all harmonics are migrating tides. Our results reveal that wave activities during SSWs are more diverse than previously realized, prompting the need for more in-depth study of tidal behavior in Earth's atmosphere. Given that tides play an important role in the vertical coupling between atmospheric regions, we suspect the SSW response of the tides should also occur broadly in the near-Earth space, for example, in the ionosphere and thermosphere.

Appendix A: Approaches for Wave Number Diagnosis

A.1. A Dual-Station Approach

Ground-based radars provided long continuous records of mesospheric winds but are available only at a limited number of sites. Radars can hardly compose a functional network for exploring the horizontal scale of global-scale waves, but do provide high spatial and temporal information on local dynamics. Efforts have been made in the past to join two zonally aligned detectors to diagnose the zonal scale of waves through analyzing the phase variations of the wave-like oscillations (e.g., Clark et al., 2002; Pogoreltsev et al., 2002; Won et al., 2003). Recently, this approach was consolidated into a compact method, called the phase differencing technique (PDT, He, Chau, Stober, et al., 2018; He, Chau, Hall, et al., 2018), in which PDT was used to explore a variety of waves. As summarized in, for esample, equation (19) in He, Chau, Stober et al. (2018), if a single wave with an unknown zonal wave number m at given frequency f is coherently detected at two longitudes λ_1 and λ_2 with amplitudes $\tilde{a}_1$ and $\tilde{a}_2$, then m has a solution,

$$m = \frac{\arg\left\{\tilde{a}_2^* \tilde{a}_1\right\} + 2C\pi}{\lambda_1 - \lambda_2} \tag{A1}$$

Here, $\tilde{a}_1$ and $\tilde{a}_2$ could be estimated from spectral analysis as in Figure 1a; and $C \in \mathbb{Z}$ represents the whole-cycle ambiguity. To deal with the ambiguity, traditional approaches required that the underlying wavelengths are long enough so that $C = 0$ (e.g., Isoda et al., 2002; Walker et al., 2004) which was released to $C \in \{-1, 0, 1\}$ through assuming $m \in \mathbb{Z}$ (e.g., He, Chau, Stober et al., 2018, equation (14)). Here, the three radars allow us to release the C further conservatively and subjectively to $C \in C_c := \{-1, 0, 1, \ldots, 10\}$. Note that the maximum possible C_c is different at harmonic as discussed in the end of the current section.

The three radars compose three combinations of radar pairs, $k = 1, 2, 3$, allowing three solutions $m_k(C)$ for each $C \in C_c$ at each frequency according to equation (A1). If only one wave m exist (namely, satisfies the single wave assumption, cf, He, Chau, Hall et al. 2018), then $m_k(C_k)$ from the three pairs should converge, namely, C_1^m, C_2^m, and C_3^m exist so that $m_1(C_1^m) = m_2(C_2^m) = m_3(C_3^m)$ or their variance $\sigma^2(m_k(C_k^m)) := \sum_k \left(m_k - \bar{m}_k\right)^2/3 = 0$. Then, C_k and m_k can be optimized through minimizing $\sigma^2(m_k)$,

$$\hat{C}_k^m = \text{argmin } \sigma^2(m_k) \tag{A2}$$

The resultant $\hat{m}_k(C_k^m)$ is displayed in Figure 1b, in which three colors, yellow, magenta and cyan, of the symbols represent $k = 1,2,3$, while the circular and triangle shapes represent $C_k^m = 0$ and 1, respectively.

In Figure 1b and at most harmonics, the separation between the cyan symbol and any of the other two is larger than the separation between the other two, which might be due to the associated longitudinal difference, that is, between Kazan and Juliusruh, is smaller that the longitudinal difference of other pairs. A smaller separation in longitude, according to equation (A1), will be associated with a larger uncertainty in the wave number estimation. Besides, in Figure 1b the estimations at S3 and S5 do not converge as good

as those at the rest of the harmonics, potentially because the relative intensity (the ratio between tidal peak and the background noise) at S3 and S5 is lower than that at other harmonics. The relative intensity might affect the maximum possible C_c defined subjectively above. For example, if we expand C_c in equation (A2) to $\{-1, 0, \ldots, 27\}$, the estimation $\hat{m}_k$ varies at S3 and S5, but not at the rest of the four harmonics.

A.2. A Triple-Station Approach

Following, for example, equation (1) in He and Chau (2019), the complex amplitude $\tilde{a}_k$ of an oscillation due to a single zonally traveling wave with wave number m detected by a radar at longitude λ_k, $k = 1, 2, 3$, could be represented as $\tilde{a}_k = \tilde{a}_0 e^{i2\pi m\lambda_k}$. The estimation of $\tilde{a}_k$ in Figure 1a allows estimating $\tilde{a}_o(m)$ at arbitrary m through a least squares regression, denoted as $\hat{\tilde{a}}_o(m)$. We estimate $\hat{\tilde{a}}_o(m)$ on a candidate grid $m \in M_s = -1, -0.9, -0.8, \ldots, 70$, and optimize m through

$$\hat{m}^T = \text{argmin} \sum_k |\tilde{a}_k - \hat{\tilde{a}}_o(m) e^{i2\pi m\lambda_k}|^2 \quad \text{(A3)}$$

where the superscript "T" denotes triple-station analysis. The optimization results are displayed in Figure 1b as white crosses. Note that similar to C_c in the previous section, M_s is preassigned subjectively, and at most harmonics the estimation will still stand in a broader M_s range.

References

Acknowledgments
This work was supported by the Deutsche Forschungsgemeinschaft (DFG, German Research Foundation) under SPP 1788 (DynamicEarth) projects CH1482/1-2 (DYNAMITE-2). Jeffrey M. Forbes acknowledges support under NSF Award AGS-1630177 to the University of Colorado Boulder. Dmitry V. Korotyshkin is supported by RFBR through Grant 18-505-12048. The authors acknowledge Tarique Siddiqui for providing the list of PVWs. The data from Mohe is provided by BNOSE (Beijing National Observatory of Space Environment), IGGCAS (Institute of Geology and Geophysics, Chinese Academy of Sciences) through the Data Center for Geophysics, National Earth System Science Data Sharing Infrastructure (http://wdc.geophys.cn). Data in this paper are available at this site (https://doi.org/10.7910/DVN/KLOGRX).

Azeem, I., Walterscheid, R. L., Crowley, G., Bishop, R. L., & Christensen, A. B. (2016). Observations of the migrating semidiurnal and quaddiurnal tides from the RAIDS/NIRS instrument. *Journal of Geophysical Research: Space Physics*, *121*, 4626–4637. https://doi.org/10.1002/2015JA022240

Chau, J. L., Goncharenko, L. P., Fejer, B. G., & Liu, H.-L. L. (2012). Equatorial and low latitude ionospheric effects during sudden stratospheric warming events: Ionospheric effects during SSW events. *Space Science Reviews*, *168*(1-4), 385–417. https://doi.org/10.1007/s11214-011-9797-5

Clark, R. R., Burrage, M. D., Franke, S. J., Manson, A. H., Meek, C. E., Mitchell, N. J., & Muller, H. G. (2002). Observations of 7-D planetary waves with MLT radars and the UARS-HRDI instrument. *Journal of Atmospheric and Solar-Terrestrial Physics*, *64*(8), 1217–1228. https://doi.org/10.1016/S1364-6826(02)00070-6

Conte, J. F., Chau, J. L., Laskar, F. I., Stober, G., Schmidt, H., & Brown, P. (2018). Semidiurnal solar tide differences between fall and spring transition times in the Northern Hemisphere. *Annales Geophysicae*, *36*(4), 999–1008. https://doi.org/10.5194/angeo-36-999-2018

Forbes, J. M., & Vincent, R. A. (1989). Effects of mean winds and dissipation on the diurnal propagating tide: An analytic approach. *Planetary and Space Science*, *37*, 197–209. https://doi.org/10.1016/0032-0633(89)90007-X

Fuller-Rowell, T., Wang, H., Akmaev, R., Wu, F., Fang, T. W., Iredell, M., & Richmond, A. (2011). Forecasting the dynamic and electrodynamic response to the January 2009 sudden stratospheric warming. *Geophysical Research Letters*, *38*, L13102. https://doi.org/10.1029/2011GL047732

Geissler, C., Jacobi, C., & Lilienthal, F. (2019). Forcing mechanisms of the quarterdiurnal tide. *Annales Geophysicae Discusses*, *2019*, 1–24. https://doi.org/10.5194/angeo-2019-145

Goncharenko, L. P., Coster, A. J., Plumb, R. A., & Domeisen, D. I. V. (2012). The potential role of stratospheric ozone in the stratosphere-ionosphere coupling during stratospheric warmings. *Geophysical Research Letters*, *39*, L08101. https://doi.org/10.1029/2012GL051261

Gong, Y., Ma, Z., Lv, X., Zhang, S., Zhou, Q., Aponte, N., & Sulzer, M. (2018). A study on the quarterdiurnal tide in the thermosphere at Arecibo during the February 2016 sudden stratospheric warming event. *Geophysical Research Letters*, *45*, 13,142–13,149. https://doi.org/10.1029/2018GL080422

Gong, Y., & Zhou, Q. (2011). Incoherent scatter radar study of the terdiurnal tide in the E-and F-region heights at Arecibo. *Geophysical Research Letters*, *38*, L15101. https://doi.org/10.1029/2011GL048318

Guharay, A., Batista, P. P., Buriti, R. A., & Schuch, N. J. (2018). On the variability of the quarter-diurnal tide in the MLT over Brazilian low-latitude stations. *Earth, Planets and Space*, *70*(1), 2337–2344. https://doi.org/10.1186/s40623-018-0910-9

Hagan, M. E., Burrage, M. D., Forbes, J. M., Hackney, J., Randel, W. J., & Zhang, X. (1999). GSWM-98: Results for migrating solar tides. *Journal of Geophysical Research*, *104*(A4), 6813–6827. https://doi.org/10.1029/1998ja900125

He, M., & Chau, J. L. (2019). Mesospheric semidiurnal tides and near-12 h waves through jointly analyzing observations of five specular meteor radars from three longitudinal sectors at boreal midlatitudes. *Atmospheric Chemistry and Physics*, *19*(9), 5993–6006. https://doi.org/10.5194/acp-19-5993-2019

He, M., Chau, J. L., Hall, C. M., Tsutsumi, M., Meek, C., & Hoffmann, P. (2018). The 16-day planetary wave triggers the SW1-tidal-like signatures during 2009 sudden stratospheric warming. *Geophysical Research Letters*, *45*, 12,631–12,638. https://doi.org/10.1029/2018GL079798

He, M., Chau, J. L., Stober, G., Hall, C. M., Tsutsumi, M., & Hoffmann, P. (2017). Application of Manley-Rowe relation in analyzing nonlinear interactions between planetary waves and the solar semidiurnal tide during 2009 sudden stratospheric warming event. *Journal of Geophysical Research: Space Physics*, *122*, 10,783–10,795. https://doi.org/10.1002/2017JA024630

He, M., Chau, J. L., Stober, G., Li, G., Ning, B., & Hoffmann, P. (2018). Relations between semidiurnal tidal variants through diagnosing the zonal wavenumber using a phase differencing technique based on two ground-based detectors. *Journal of Geophysical Research: Atmospheres*, *123*, 4015–4026. https://doi.org/10.1002/2018JD028400

Hedlin, M. A. H., de Groot-Hedlin, C. D., Forbes, J. M., & Drob, D. P. (2018). Solar terminator waves in surface pressure observations. *Geophysical Research Letters*, *45*, 5213–5219. https://doi.org/10.1029/2018GL078528

Hibbins, R. E., Espy, P. J., Orsolini, Y. J., Limpasuvan, V., & Barnes, R. J. (2019). SuperDARN observations of semidiurnal tidal variability in the MLT and the response to sudden stratospheric warming events. *Journal of Geophysical Research: Atmospheres*, *124*, 4862–4872. https://doi.org/10.1029/2018JD030157

Isoda, F., Tsuda, T., Nakamura, T., Murayama, Y., Igarashi, K., Vincent, R. A., et al. (2002). Long-period wind oscillations in the mesosphere and lower thermosphere at Yamagawa (32°N, 131°E), Pontianak (0°N, 109°E) and Christmas Island (2°N, 157°W). *Journal of Atmospheric and Solar-Terrestrial Physics*, *64*(8-11), 1055–1067. https://doi.org/10.1016/S1364-6826(02)00057-3

Jacobi, C., Krug, A., & Merzlyakov, E. (2017). Radar observations of the quarterdiurnal tide at midlatitudes: Seasonal and long-term variations. *Journal of Atmospheric and Solar-Terrestrial Physics*, *163*, 70–77. https://doi.org/10.1016/j.jastp.2017.05.014

Korotyshkin, D., Merzlyakov, E., Jacobi, C., Lilienthal, F., & Wu, Q. (2019). Longitudinal MLT wind structure at higher mid-latitudes as seen by meteor radars at central and Eastern Europe (13°E/49°E). *Advances in Space Research*, *63*(10), 3154–3166. https://doi.org/10.1016/j.asr.2019.01.036

Lilienthal, F., & Jacobi, C. (2019). Nonlinear forcing mechanisms of the terdiurnal solar tide and their impact on the zonal mean circulation. *Annales Geophysicae Discusses*, 1–18. https://doi.org/10.5194/angeo-2019-37

Limpasuvan, V., Orsolini, Y. J., Chandran, A., Garcia, R. R., & Smith, A. K. (2016). On the composite response of the MLT to major sudden stratospheric warming events with elevated stratopause. *Journal of Geophysical Research: Atmospheres*, *121*, 4518–4537. https://doi.org/10.1002/2015JD024401

Lindzen, R. S., & Hong, S.-S. (1974). Effects of mean winds and horizontal temperature gradients on solar and lunar semidiurnal tides in the atmosphere (Vol. *31*, No. 5). https://doi.org/10.1175/1520-0469(1974)031<1421:eomwah>2.0.co;2

Liu, H. L., Wang, W., Richmond, A. D., & Roble, R. G. (2010). Ionospheric variability due to planetary waves and tides for solar minimum conditions. *Journal of Geophysical Research*, *115*, A00G01. https://doi.org/10.1029/2009JA015188

Liu, M. H., Xu, J. Y., Yue, J., & Jiang, G. Y. (2015). Global structure and seasonal variations of the migrating 6-h tide observed by SABER/TIMED. *Science China Earth Sciences*, *58*(7), 1216–1227. https://doi.org/10.1007/s11430-014-5046-6

Lomb, N. R. (1976). Least-squares frequency analysis of unequally spaced data. *Astrophysics and Space Science*, *39*(2), 447–462. https://doi.org/10.1007/BF00648343

Miyahara, S., & Forbes, J. M. (1991). Interactions between gravity waves and the diurnal tide in the mesosphere and lower thermosphere. *Journal of the Meteorological Society of Japan*, *69*(5), 523–531. https://doi.org/10.2151/jmsj1965.69.5_523

Miyoshi, Y., Fujiwara, H., Forbes, J. M., & Bruinsma, S. L. (2009). Solar terminator wave and its relation to the atmospheric tide. *Journal of Geophysical Research*, *114*, A07303. https://doi.org/10.1029/2009JA014110

Pancheva, D., Merzlyakov, E., Mitchell, N. J., Portnyagin, Y., Manson, A. H., Jacobi, C., et al. (2002). *Global-scale tidal variability during the PSMOS campaign of June-August 1999: Interaction with planetary waves* (Vol. 64, pp. 1865–1896). https://doi.org/10.1016/S1364-6826(02)00199-2

Pedatella, N. M., & Forbes, J. M. (2010). Evidence for stratosphere sudden warming-ionosphere coupling due to vertically propagating tides. *Geophysical Research Letters*, *37*, L11104. https://doi.org/10.1029/2010GL043560

Pedatella, N. M., Liu, H. L., Sassi, F., Lei, J., Chau, J. L., & Zhang, X. (2014). Ionosphere variability during the 2009 SSW: Influence of the lunar semidiurnal tide and mechanisms producing electron density variability. *Journal of Geophysical Research: Space Physics*, *119*, 3828–3843. https://doi.org/10.1002/2014JA019849

Pogoreltsev, A. I., Pancheva, D., & Mitchell, N. J. (2002). Secondary planetary waves in the middle atmosphere: Numerical simulation and analysis of the neutral wind data. *Journal of Atmospheric and Solar-Terrestrial Physics*, *64*(8-11), 1251–1261. https://doi.org/10.1016/S1364-6826(02)00039-1

Reed, R. (1963). On the cause of the stratospheric sudden warming phenomenon. *Meteorological Abhand*, *36*, 315–334.

Riggin, D. M., Meyer, C. K., Fritts, D. C., Jarvis, M. J., Murayama, Y., Singer, W., et al. (2003). MF radar observations of seasonal variability of semidiurnal motions in the mesosphere at high northern and southern latitudes. *Journal of Atmospheric and Solar-Terrestrial Physics*, *65*(4), 483–493. https://doi.org/10.1016/S1364-6826(02)00340-1

Sathishkumar, S., & Sridharan, S. (2013). Lunar and solar tidal variabilities in mesospheric winds and EEJ strength over Tirunelveli (8.7°N, 77.8°E) during the 2009 major stratospheric warming. *Journal of Geophysical Research: Space Physics*, *118*, 533–541. https://doi.org/10.1029/2012JA018236

Scherhag, R. (1952). Die explosionsartigen Stratosphärenerwärmungen des Spätwinters 1951/52. *Berichte des Dtsch. Wetterdienstes der US-Zone*, *6*(38), 51–63.

Siddiqui, T. A., Maute, A., & Pedatella, N. M. (2020). On the importance of interactive ozone chemistry in Earth-system models for studying mesophere-lower thermosphere tidal changes during sudden stratospheric warmings. *Journal of Geophysical Research: Space Physics*, *124*, 10,690–10,707. https://doi.org/10.1029/2019JA027193

Siddiqui, T. A., Stolle, C., Lühr, H., & Matzka, J. (2015). On the relationship between weakening of the northern polar vortex and the lunar tidal amplification in the equatorial electrojet. *Journal of Geophysical Research: Space Physics*, *120*, 10,006–10,019. https://doi.org/10.1002/2015JA021683

Singer, W., Hoffmann, P., Kishore Kumar, G., Mitchell, N. J., & Matthias, V. (2013). Atmospheric coupling by gravity waves: Climatology of gravity wave activity, mesospheric turbulence and their relations to solar activity. In F.-J. Lübken (Ed.), *Climate weather sun-earth systeme highlights from a prior. progr.* (pp. 409–427). Dordrecht: Springer Netherlands. https://doi.org/10.1007/978-94-007-4348-9_22

Smith, A. K. (2012). Global dynamics of the MLT. *Surveys in Geophysics*, *33*(6), 1177–1230. https://doi.org/10.1007/s10712-012-9196-9

Smith, A. K., Pancheva, D. V., & Mitchell, N. J. (2004). Observations and modeling of the 6-hour tide in the upper mesosphere. *Journal of Geophysical Research*, *109*, D10105. https://doi.org/10.1029/2003JD004421

Sridharan, S., Sathishkumar, S., & Gurubaran, S. (2012). Variabilities of mesospheric tides during sudden stratospheric warming events of 2006 and 2009 and their relationship with ozone and water vapour. *Journal of Atmospheric and Solar-Terrestrial Physics*, *78-79*, 108–115. https://doi.org/10.1016/j.jastp.2011.03.013

Truskowski, A. O., Forbes, J. M., Zhang, X., & Palo, S. E. (2014). New perspectives on thermosphere tides: 1. Lower thermosphere spectra and seasonal-latitudinal structures. *Earth, Planets and Space*, *66*(1), 1–17. https://doi.org/10.1186/s40623-014-0136-4

Walker, S. N., Sahraoui, F., Balikhin, M. A., Belmont, G., Pinçon, J. L., Rezeau, L., et al. (2004). A comparison of wave mode identification techniques. *Annales Geophysicae*, *22*(8), 3021–3032. https://doi.org/10.5194/angeo-22-3021-2004

Won, Y. I., Wu, Q., Cho, Y. M., Shepherd, G. G., Killeen, T. L., Espy, P. J., et al. (2003). Polar cap observations of mesospheric and lower thermospheric 4-hour waves in temperature. *Geophysical Research Letters*, *30*(7), 10–13. https://doi.org/10.1029/2002GL016364

Xiong, J., Wan, W., Ding, F., Liu, L., Ning, B., & Niu, X. (2013). Coupling between mesosphere and ionosphere over Beijing through semidiurnal tides during the 2009 sudden stratospheric warming. *Journal of Geophysical Research: Space Physics*, *118*, 2511–2521. https://doi.org/10.1002/jgra.50280

Xu, J., Smith, A. K., Jiang, G., Yuan, W., & Gao, H. (2012). Features of the seasonal variation of the semidiurnal, terdiurnal and 6-h components of ozone heating evaluated from Aura/MLS observations. *Annales Geophysicae*, *30*(2), 259–281. https://doi.org/10.5194/angeo-30-259-2012

Yu, Y., Wan, W., Ning, B., Liu, L., Wang, Z., Hu, L., & Ren, Z. (2013). Tidal wind mapping from observations of a meteor radar chain in December 2011. *Journal of Geophysical Research: Space Physics*, *118*, 2321–2332. https://doi.org/10.1029/2012JA017976

Zülicke, C., & Becker, E. (2013). The structure of the mesosphere during sudden stratospheric warmings in a global circulation model. *Journal of Geophysical Research: Atmospheres*, *118*, 2255–2271. https://doi.org/10.1002/jgrd.50219

Zhang, X., & Forbes, J. M. (2014). Lunar tide in the thermosphere and weakening of the northern polar vortex. *Geophysical Research Letters*, *41*, 8201–8207. https://doi.org/10.1002/2014GL062103